JACS
JOURNAL OF THE AMERICAN CHEMICAL SOCIETY
pubs.acs.org/JACS
Article

Mapping Vibronic Dynamics of Ultrafast Intersystem Crossing in an Earth-Abundant Ligand-Field Excited Complex

Jing Yang,[¶] Panpan Zhang,[¶] Zihui Liu,[¶] Michael Penny, Sara Mosca, Junhua Zhou, Vandana Tiwari, Benjamin G. Davis, Fulu Zheng,* Hong-Guang Duan,* and Ajay Jha*

Cite This: *J. Am. Chem. Soc.* 2026, 148, 1977−1988

ABSTRACT: Intersystem crossing (ISC) is a central nonradiative pathway in transition-metal complexes, critically shaping their behavior in photocatalysis and optoelectronics. In 3d metal systems, ligand-field (LF, d−d) excited states are especially important, yet the mechanisms governing their ISC remain obscure because LF transitions are commonly masked by intense metal-to-ligand charge-transfer (MLCT) bands. This knowledge gap is significant, as LF states frequently participate in deactivation channels and directly influence the photochemical reactivity. Here, we focus on unraveling the ultrafast ISC dynamics in a carefully chosen model system with a simplified electronic structure: cobalt(III)-acetylacetonate, ($[Co(acac)_3]$), a d^6 low-spin complex. Upon selective $^1A_1 \rightarrow {}^1T_1$ ligand-field excitation promoting a $t_{2g} \rightarrow e_g{}^*$ electron, heterodyne-detected transient grating measurements with ∼10 fs pulses reveal vibrational coherences decaying in ∼50 fs, matching ISC dynamics. Fourier analysis reveals both low- and high-frequency vibrational modes associated with Co−O stretching and Co−O−C bending that actively mediate the spin-state transition. Complementary two-dimensional electronic spectroscopy (2DES) disentangles overlapping signals and localizes vibrational activity near the $^1T_1$ excited-state absorption. Density functional theory (DFT) and GPU-accelerated hierarchy equation of motion (HEOM) calculations confirm that vibronic coupling, in concert with spin−orbit coupling (SOC), enables rapid singlet-to-triplet conversion via dynamic modulation of excited-state energies and reorganization along key nuclear coordinates. These results reveal that following LF excitation vibronic coupling plays an important role in reshaping excited-state potential energy surfaces and facilitating ISC in systems where SOC alone is weak. This work establishes a mechanistic foundation for understanding and controlling excited-state pathways in LF-dominated 3d transition-metal complexes.

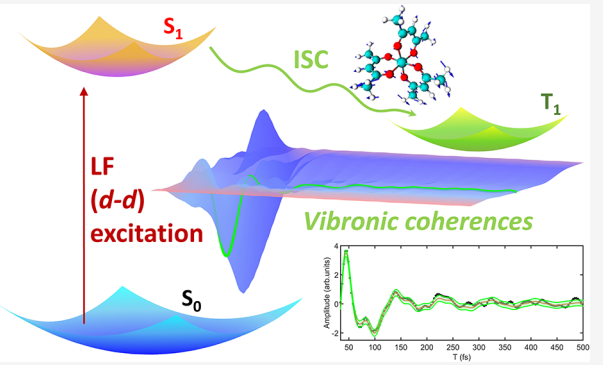

INTRODUCTION

Intersystem crossing is defined as a transition between electronic states of different spin multiplicities, typically from a singlet state to a triplet state. The ability to efficiently undergo ISC is a key factor in the design of materials for photocatalytic and optoelectronic applications.[1−5] Moreover, ISC is central to the photostability and the performance of the photosensitizer used in photodynamic therapy, as it governs the formation of reactive oxygen species.[6−8] ISC is generally slow due to the spin-forbidden nature of the transition. However, in transition-metal complexes, strong SOC inherent to heavy-metal atoms significantly accelerates this process by mixing states of different spin multiplicities and thereby making ISC transitions partially allowed. Thus, SOC provides the electronic mechanism for mixing states, which increases strongly with atomic number ($\propto Z^4$). Vibronic coupling is another mechanism that enhances the ISC rate by mixing electronic and vibrational states. This can be particularly important when SOC is weak, acting as a "bridge" to couple singlet and triplet states. Understanding the interplay of SOC and vibronic coupling during ISC in these complexes is therefore key to unraveling the electronic and spin dynamics of excited states with broad potential function.[9]

The dynamics of ISC and subsequent relaxation pathways in transition-metal complexes have been extensively investigated,[10−17] particularly for synthetically valued 2nd- and 3rd-row elements such as Ru(II) and Ir(III), where strong SOC renders ISC extremely fast, often faster than vibrational relaxation, thereby ensuring efficient population of triplet states. By contrast, first-row transition-metal complexes exhibit weaker SOC and possess low-lying LF excited states that are typically both spin- and Laporte-forbidden, leading to rapid nonradiative decay and short excited-state lifetimes.[18−21]

Received: November 17, 2025
Revised: December 13, 2025
Accepted: December 16, 2025
Published: December 24, 2025

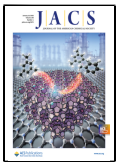

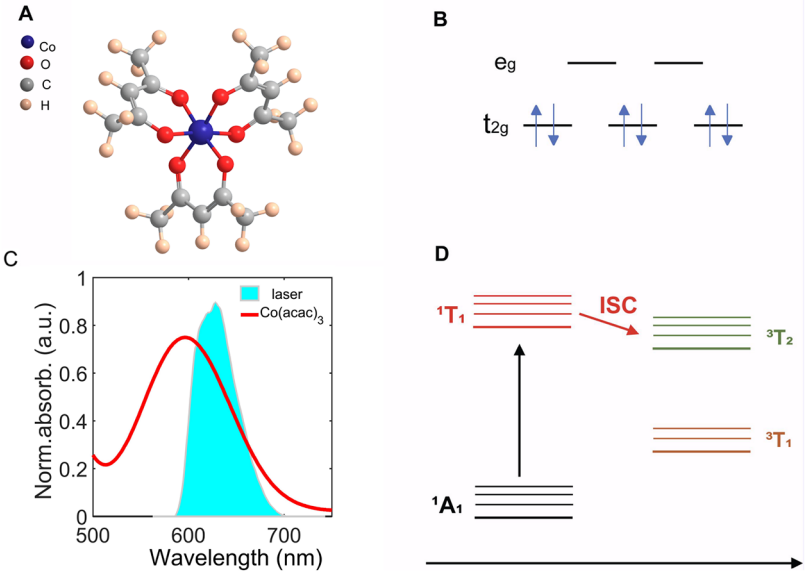

Figure 1. Intersystem crossing following ligand-field excitation in $[Co(acac)_3]$: (A). The molecular structure of the tris(acetylacetonato)cobalt(III) complex features three acetylacetonato ligands, each binding in a bidentate fashion to the cobalt center, forming an octahedral geometry. (B). $[Co(acac)_3]$ is a low-spin complex, where all d^6 electrons are paired in the lower-energy t_{2g} orbitals. (C). Ligand-field absorption features associated with $^1A_1$ to $^1T_1$ transition is centered at 596 nm. Laser spectral profile used in this study is presented as a blue-shaded spectrum; (D). Schematic representing ground state electronic energy level, $^1A_1$ with excited state $^1T_1$. The photoexcitation from the spin-allowed $^1A_1$ to $^1T_1$ transition is followed by intersystem crossing to the $^3T_2$ state, which is the primary focus of this study.

These intrinsic electronic features have therefore historically limited the photophysical performance of 3d metal systems and thus their utility, despite their chemical versatility and abundance. This has typically prevented their use in, for example, driving potentially powerful single electron transfer chemistries with organic reactants. Nevertheless, recent efforts have focused on understanding how vibronic coupling and molecular geometry modulate ISC efficiency in such complexes.[22−29] Ultrafast ISC dynamics in transition-metal systems have now been shown to arise from a subtle interplay between vibrational motion and SOC, providing a comprehensive theoretical framework for this spin-vibronic mechanism.[30] A recent perspective has summarized case studies spanning first- to third-row metals, elucidating how specific normal modes drive early-time photophysics.[31] Complementary quantum-dynamical simulations of a Mn(I) complex highlight the need to include higher excited states to reproduce coherence-driven ISC,[32] and a recent study on a Pt(II) complex revealed a clear spin-vibronic ISC pathway even in systems with inherently strong SOC.[33]

Building on these insights, cobalt(III) complexes offer an especially intriguing platform for probing such spin-vibronic interactions. The photophysics and photochemistry of Co(III) complexes have only recently gained attention, and comparatively few examples have been investigated.[34−39] In most of these systems, excitation to MLCT is followed by ISC crossing. However, our understanding of ISC pathways following LF excitation remains limited, primarily because LF excitations are often spectroscopically overshadowed by intense and lower-energy MLCT transitions, especially in 3d transition-metal complexes. An important exception arises in a few Co(III) complexes, where ligand-field transitions are significantly frequency-shifted, allowing for the direct and selective excitation of LF states. This spectral window has recently been exploited in ultrafast spectroscopic studies.[40] While these studies provide valuable initial insights into the time scales of state-to-state transitions, a comprehensive mechanistic understanding of ISC driven by direct LF excitation in Co(III) and related 3d metal complexes still remains elusive, particularly regarding the respective contributions of SOC and vibronic coupling in facilitating these processes. Addressing this knowledge gap is not only fundamental to advancing the photophysics of earth-abundant transition metals but also would enable potential design for sustainable photochemical reactivity, luminescence, and energy conversion processes using 3d metal platforms.

Here, we have studied $[Co(acac)_3]$ as a model molecule to explore the nature of ISC dynamics after subjecting the system to ligand-field excitation by capturing the vibronic dynamics. The ligand acac, although generally considered an intermediate ligand, creates a sufficiently strong ligand field with Co(III) to cause a significant splitting of the d-orbitals, leading to a low-spin complex. Therefore, in the resulting complex, $[Co(acac)_3]$, all $3d^6$ electrons are paired in the lower-energy t_{2g} orbitals. Previous studies on this complex proposed the ultrafast rise of triplet states, but the exact time scale could not be effectively determined using limited time resolution. Here, we examine the process of ISC in $[Co(acac)_3]$ using a combination of ultrafast heterodyne-detected transient grating (TG) and 2DES. Notably, we observe vibrational coherences persisting for ∼50 fs in the transient signals that coincide with the onset of ISC. This now suggests that nuclear motions on the ∼100 fs time scale actively assist the ultrafast singlet-to-triplet conversion, a hypothesis that we explore through correlated experiments and spin-vibronic simulations. Quantum chemistry calculations reveal the significant strength of SOC and the vibronic couplings of the intra- and intermolecular modes, which markedly modulate the electronic coupling between the singlet and triplet states. With the assistance of SOC, the strong vibronic couplings of intramolecular vibrations open effective channels that enhance the population transfer in the ISC of $[Co(acac)_3]$.

https://doi.org/10.1021/jacs.5c20395
J. Am. Chem. Soc. 2026, 148, 1977−1988

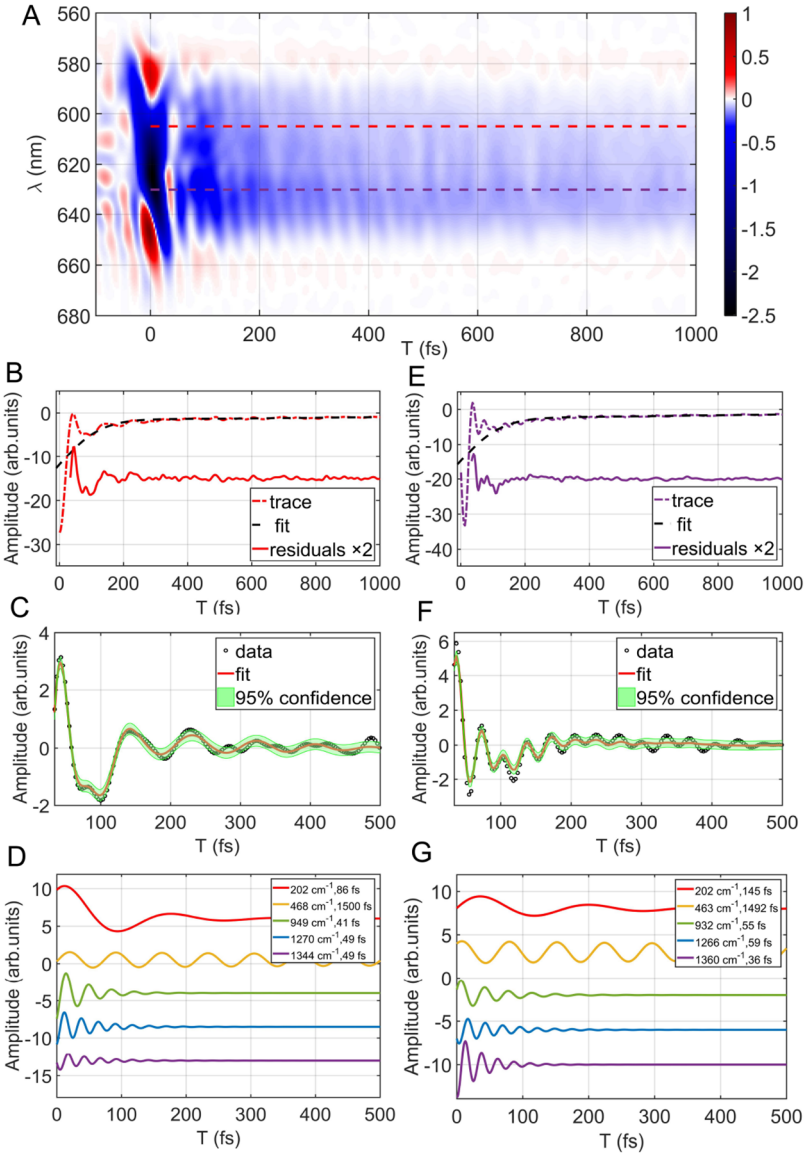

Figure 2. (A). TG spectrum of the $[Co(acac)_3]$ complex measured at room temperature. The negative magnitude (blue in the color bar) shows the excited-state absorption (ESA) signal. Two selected traces are plotted as colored dashed lines in (A). The selected time-resolved traces are plotted as dashed lines in (B, E), respectively. The fitting curves and residuals are plotted as black dashed lines and colored solid lines. The fitting results of residuals and 95% of boundaries are shown in (C, F), respectively. The resolved modes with oscillatory dynamics are shown in (D, G).

RESULTS

$[Co(acac)_3]$ (Figure 1(A)) is a low-spin complex, where all d^6 electrons are paired in the lower-energy t_{2g} orbitals (Figure 1(B)). The electronic transition ($^1A_1 \rightarrow {}^1T_1$) with an absorption peak at ∼600 nm is marked (Figure 1(C,D)). We performed broadband transient absorption spectroscopy at room temperature (300 K) exciting the $^1A_1 \rightarrow {}^1T_1$ electronic transition and probing within the spectral range of 370 to 520 nm (Supporting Figure S1(a)). These measurements complement the findings reported by Ferrari et al., who investigated a different probe frequency range and similarly observed a biexponential decay in the excited-state absorption features.[38] The initial decay time constant, attributed to ISC, was found to be limited by the experimental time resolution of ∼200 fs. To elucidate the early ISC time constant and the associated vibrational dynamics, we employed TG spectroscopy using ∼10 fs pulses.

Transient Grating Spectroscopy. TG spectroscopy, being phase-sensitive, involves generating an interference pattern between two pump pulses and detecting the resulting diffraction signal from the sample. This phase sensitivity enables the isolation of coherent oscillations, such as those arising from vibrational or electronic coherence, by effectively distinguishing them from incoherent background signals.[41,42] We measured the absorption spectrum (depicted as a red solid line) and compared it with the laser spectrum used in this study (illustrated as a blue-shaded region), as presented in Figure 1(C). The measured TG spectrum is shown in Figure 2(A), covering a detection time window of up to 3 ps with probe wavelengths ranging from 560 to 680 nm. The negative magnitude signifies excited-state absorption (ESA) features. At T = 0 fs, a strong signal is observed across all detection wavelengths, which rapidly decays within the first 100 fs. Additionally, we detect an ESA signal throughout the detection range of 580 to 660 nm, albeit with a relatively weak intensity.

https://doi.org/10.1021/jacs.5c20395
J. Am. Chem. Soc. 2026, 148, 1977−1988

Table 1. Fitting Parameters of $Co(acac)_3$

λ = 605 nm				λ = 635 nm			
A (a.u)	T (fs)	ω (cm^{-1})	Φ (rad)	A (a.u)	T (fs)	ω (cm^{-1})	Φ (rad)
1.44	59.73	108.1	1.081	0.8649	167.9	99.93	2.512
−5.211	86.36	202.9	−2.316	1.849	145.1	202.8	0.03659
0.7037	402	234	2.467	0.5	402.6	236.3	1.73
1.05382	1500	467.8	0.1994	1.2741	1492	463	0.886
3.877	40.51	949.4	−1.088	1.928	55.96	932.1	0.3368
2.436	49.56	1270	1.289	−1.676	59.2	1266	0.6552
1.354	49.16	1344	3.345	3.849	35.45	1360	−1.852

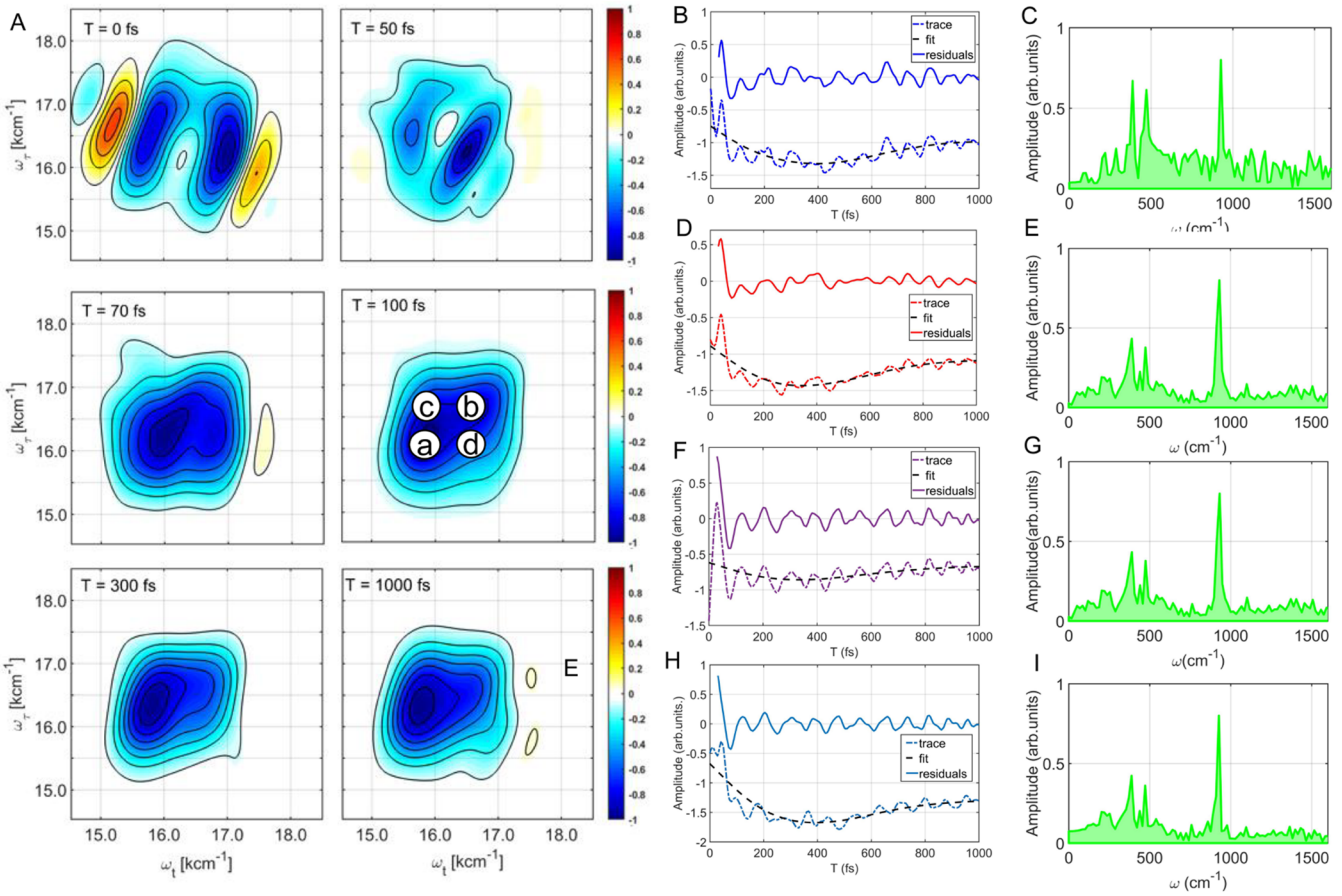

Figure 3. (A) Measured two-dimensional electronic spectra (2DES) with selected waiting times of 0, 50, 70, 100, 300, and 1000 fs, respectively. The selected peaks are marked with a, b, c, and d in 2DES map of T = 100 fs. The decay traces, fitting curves, and residuals are plotted in (B, D, F, H). The FFT resulted data and resolved vibrational frequencies are shown in (C, E, G, I).

Coherent dynamics can be inferred through oscillations in the contour lines of the TG spectrum, despite the relatively weak ESA optical signals. To facilitate the phasing procedure and retrieve the real part of the TG spectrum, we also measured the transient absorption spectrum, as detailed in the Supporting Information, Figure S1(b).

To further investigate the associated coherent dynamics, we extracted the amplitude variations at selected wavelengths and plotted the corresponding time-resolved traces in Figure 2(B, E), represented by red and purple dashed lines, respectively. To analyze these traces in greater detail, we performed a fitting procedure using one or two exponential functions to model the kinetic behavior. The fitted kinetics were subsequently subtracted, allowing us to obtain the residuals, which are displayed as red and purple solid lines in Figure 2(B, E), respectively. To elucidate the time-evolved coherences, we conducted an in-depth data analysis. Initially, the extracted residuals were plotted as black circles in Figure 2(C, F) to visually represent the oscillatory features. To accurately characterize these oscillations, we applied an exponentially decaying sine function fitting procedure to determine their frequencies and corresponding lifetimes. The fitting process was initiated using seven frequency components: 100, 200, 240, 470, 940, 1260, and 1350 cm^{-1}, which were previously identified through Fourier transform analysis. Notably, these initial frequency estimates are consistent with theoretical predictions and experimentally measured Raman spectrum of the complex (see Figure S3). Through this methodology, we achieved an optimal fit (R^2 > 0.97), indicating excellent agreement between the fitted model (represented by the red solid line) and the experimentally obtained residuals (Figure 2(C)) (SI, Section IV). The resolved vibrational coherence

https://doi.org/10.1021/jacs.5c20395
J. Am. Chem. Soc. 2026, 148, 1977−1988

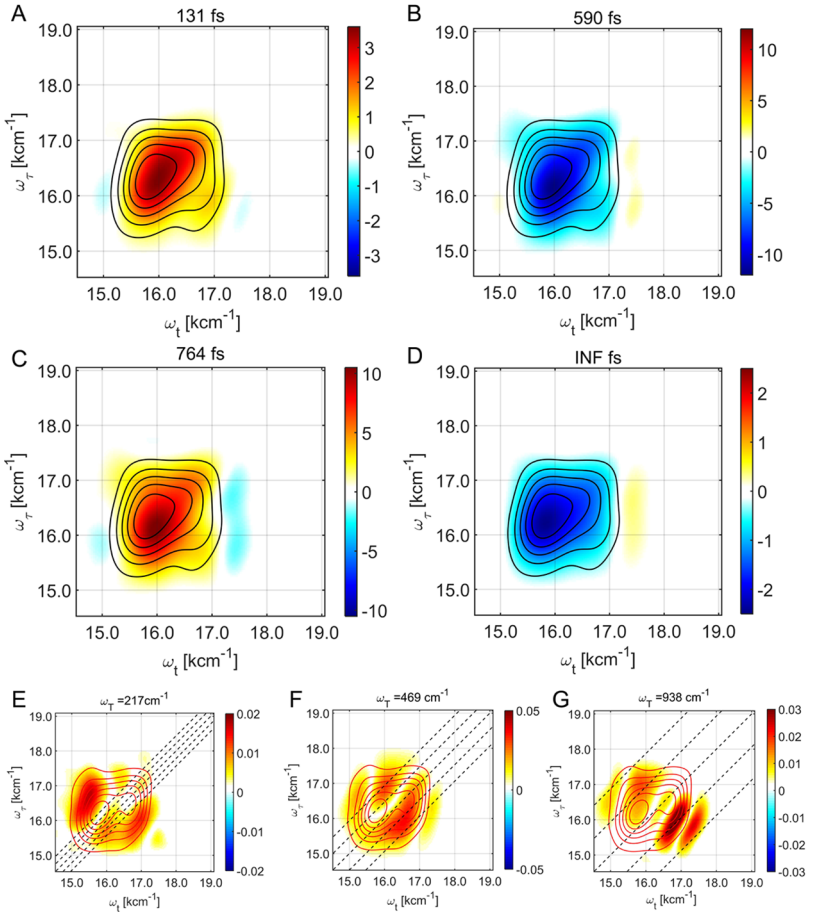

Figure 4. 2D decay-associated spectra (DAS) of the $[Co(acac)_3]$ complex (A–D) with decay lifetimes of 131 fs, 590 fs, 764 fs, and INF components. 2D vibrational maps after Fourier transform of 3D residuals (E–G) with resolved vibrational frequencies 217, 469, and 938 cm^{-1}, respectively.

components (Figure 2(D)) show frequency values of 202, 468, 949, 1270, and 1344 cm^{-1}. Beyond resolving these vibrational frequencies, this analysis also enabled determination of their lifetimes (Table 1). Specifically, the coherence at 202 cm^{-1} exhibits a strong oscillatory amplitude with a lifetime of 86 fs, completing approximately two oscillation cycles before decaying entirely within 300 fs. The mode at 468 cm^{-1}, although of comparatively lower magnitude, persists significantly longer with a lifetime of 1500 fs. Additionally, the 949 cm^{-1} mode demonstrates a relatively strong magnitude but a short lifetime of 41 fs, allowing for approximately three oscillation cycles before complete decay. Furthermore, two high-frequency modes at 1270 and 1340 cm^{-1} were observed, each with short lifetimes of 50 fs, enabling several oscillation periods before decaying within 200 fs. Apart from these main vibrational components, we also identified two additional modes at 108 and 234 cm^{-1}, with respective lifetimes of 59 and 402 fs (Figures S5 and S7). The identification of these vibrational coherences and their lifetimes provides crucial insights into the underlying quantum dynamics, demonstrating distinct oscillatory behaviors and decay characteristics across different vibrational modes.

We extended the same data treatment methodology in Figure 2(E),(F),(G), with excellent agreement between the experimental data (represented by black circles) and the corresponding fitted curves (red solid lines) to resolve vibrational frequencies and their respective lifetimes systematically. We identified a low-frequency vibrational mode at 202 cm^{-1}, exhibiting a time scale of 145 fs (Figure 2(G)). Furthermore, vibrational modes with frequencies of 463, 932, 1266, and 1360 cm^{-1} were observed with lifetimes of 1492, 55, 59, and 36 fs, respectively. This analysis confirms that the key vibrational coherences are characterized by well-defined lifetimes, all of which decay within 2 ps. Such findings suggest that the identified vibrational modes and their associated coherences dissipate within the characteristic time scale of population transfer during the ISC process in the cobalt complex.

Two-Dimensional Electronic Spectroscopy. To examine the origins of the observed vibronic coherences, we performed 2DES and analyzed the spectra at selected waiting times. The 2DES technique effectively reduces inhomogeneous broadening, enabling a more accurate investigation of dynamic processes.[43−48] The measured 2DES, including the total and real components, are presented in Figure 3(A) for waiting times of T = 0, 50, 70, 100, 300, and 1000 fs. At T = 0 fs, the 2DES spectrum exhibits a strong main peak with a negative magnitude. Additionally, both main and cross peaks, displaying negative and positive magnitudes, suggest the presence of overlapping multipulse interactions. This results in an indistinct spectral feature at T = 0 fs, making its direct interpretation challenging. However, at T = 50 fs, the measured 2DES spectrum reveals four distinct main and cross peaks, which can be attributed to the decaying signal of

https://doi.org/10.1021/jacs.5c20395
J. Am. Chem. Soc. 2026, 148, 1977−1988

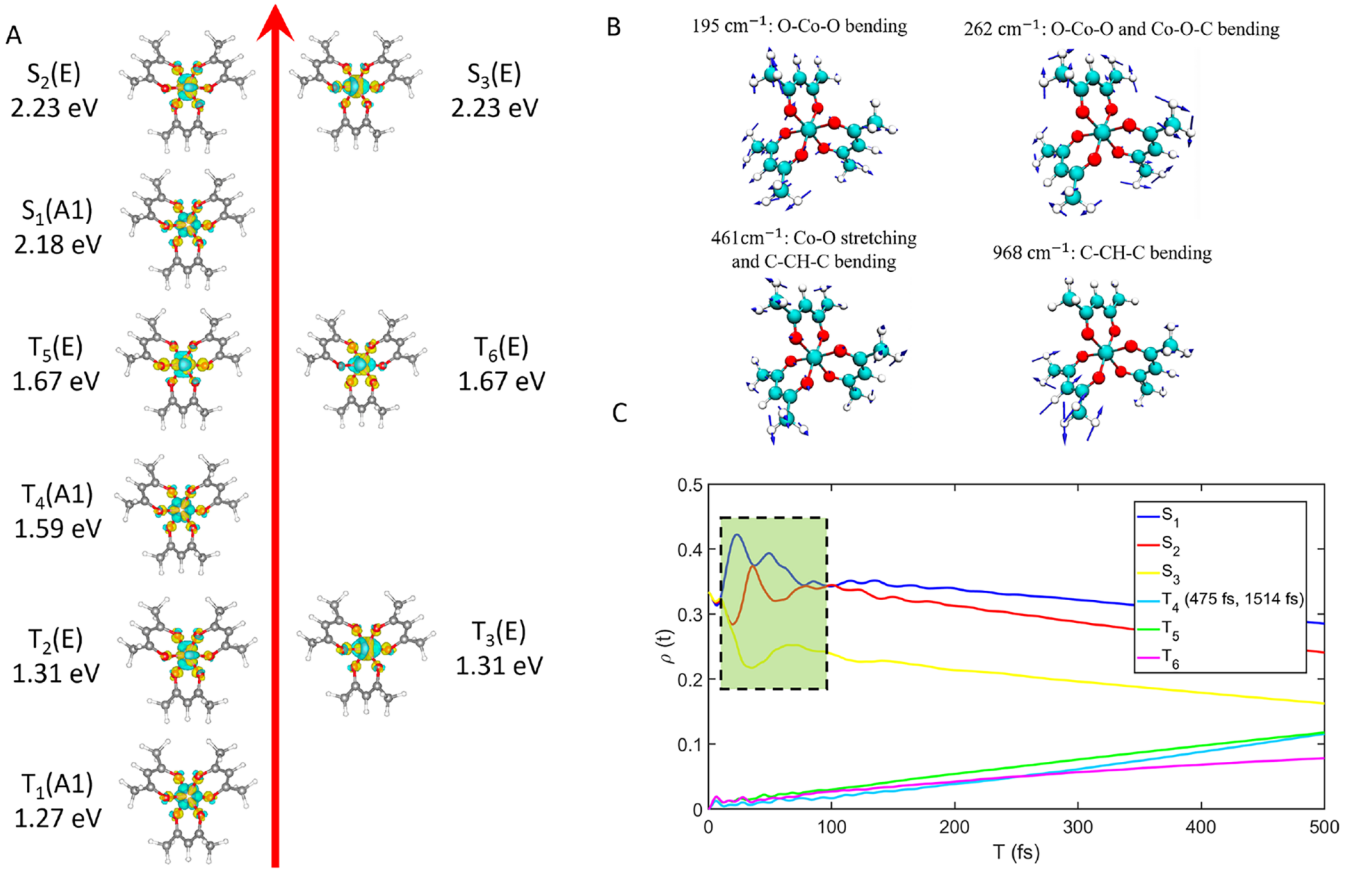

Figure 5. (A) Energies, symmetries (in parentheses), and charge density differences of the excited states of the molecule. Molecular vibrations at 195, 262, 461, and 968 cm^{-1} are presented in (B). The population dynamics of intersystem crossing from singlet to triple states are plotted in (C). Calculated population dynamics are obtained with initial density matrix with 33% of S_1 to S_3 singlet electronic states. The exponential fit shows the time scales of 475 and 1514 fs for the rise of the triplet, T_4.

the substrate and the influence of pulse overlap effects. The actual spectral contributions from the cobalt complex, free from substrate interference signal (nonresonant signal from the quartz cuvette and solvent), are represented as blue peaks in the 2DES at T = 50 fs. At T = 70 fs, the 2DES spectrum prominently features a broadband (blue) peak at (ω_τ, ω_t) = (16500, 16500) cm^{-1}. Moreover, multiple cross peaks become clearly distinguishable at this waiting time, further revealing the underlying coherent dynamics. The 2DES spectra at T = 100, 300, and 1000 fs (Figure 3(A)) consistently exhibit a central blue peak with a strong negative magnitude indicative of a pronounced ESA signature. Given the lifetime of the signal, it is assigned to triplet state absorption, and thus, singlet-to-triplet ISC dynamics. It is noteworthy that beyond T > 300 fs, the spectral features of the 2DES do not exhibit significant changes with increasing waiting time. This suggests that the dominant optical signatures of ISC remain stable beyond this time scale, indicating the completion of all primary population transfer dynamics.

To analyze the transfer timescale and the associated vibrational coherence, we selected four main and cross peaks from the 2DES spectra at T = 100 fs, as marked in Figure 3(A). These peaks are labeled as "a", "b", "c", and "d" in the measured 2DES. To examine their temporal evolution, we extracted the time-dependent magnitude of each peak and plotted the corresponding time-resolved traces in Figure 3(B), (D),(F),(H), represented by colored dashed lines. Subsequently, an exponential fitting procedure was applied to determine the kinetic components, and the resulting residuals were plotted as colored solid lines in the same figures. From this analysis, we determined the timescales of population transfer for each trace, with a detailed description provided in the SI. For peak "a", we identified two timescales of population transfer: 196 and 750 fs; that again could be attributed to singlet-to-triplet ISC (see Figure S8 in the SI). These values show excellent agreement with theoretical calculations (as discussed in the Theoretical Calculationsection). The timescales for the remaining peaks are presented in Figure 3(D), (F), (H), further supporting the population dynamics observed in the system. Additionally, we performed a Fourier transform of the residuals to extract the vibrational coherence. This identified vibrational modes and their corresponding frequencies (Figure 3(C), (E), (G), (I)) with well-resolved peaks. The results are consistent with those obtained from TG spectroscopy. In this way, by leveraging the optical measurements from 2DES, we were able to disentangle the origins of vibrational coherence more effectively by resolving them within well-separated main and cross peaks. A comprehensive discussion of the differences in optical measurement techniques and their respective frequency resolutions is provided in the SI (Section IX).

Next, we examined the population dynamics of 2DES by a global fitting approach (SI Section VI). The resulting data after global fit (Figure 4(A–D)) gave time scales of 131, 590, and 764 fs and infinite components. The two-dimensional (2D) decay-associated spectrum (DAS) of the fastest component

https://doi.org/10.1021/jacs.5c20395
J. Am. Chem. Soc. 2026, 148, 1977−1988

(Figure 4(A)) presents a distinct maximum in the center of the spectrum, which marks the central spectral position of the 2DES. This manifests decay dynamics of 2DES at the corresponding spectroscopic coordinates with a resolved time scale, τ with a fast decay component in 2DES of lifetime 131 fs. Thus, the 2D decay magnitude excellently matched the profile of 2DES. Moreover, as a slower decay component with a time scale of 590 fs, Figure 4(B) presents a strong minimum (blue) with good agreement with the contour of the 2DES. This component revealed a slower increasing amplitude in the 2DES with a lifetime of 590 fs. We also detected the third component of DAS with a lifetime of 764 fs (Figure 4(C) with a positive (red) main peak and some resolved negative (blue) side peaks). Finally, we also obtain a 2DDAS with an infinite timescale (Figure 4(D)). This negative magnitude indicates slow-increasing dynamics to zero in the 2DES.

To further resolve the vibrational coherence in 2DES, we extracted the three-dimensional (3D) residuals by subtracting the kinetic components from the full 3D data set of 2DES. A Fourier transform was then performed along waiting time T to obtain 2D vibrational maps as a function of ω_T. The resulting vibrational maps (Figure 4(E−G)) correspond to vibrational frequencies of 217, 469, and 938 cm^{-1}. The other two 2D vibrational maps with high frequencies of 1257 and 1357 cm^{-1} are presented in the SI (see Figure S2 in the SI). The resolved vibrational modes exhibit excellent agreement with those identified in the TG spectroscopy analysis. A detailed discussion comparing the optical measurement techniques of TG and 2DES, including their respective frequency resolutions, is provided in the SI (Section IX). The 2D vibrational map at ω_T = 217 cm^{-1} reveals two distinct positive side peaks localizing at (ω_τ, ω_t) = (16500, 15200) and (16000, 17000) cm^{-1} (Figure 4(E)). Notably, the 2D vibrational map at 469 cm^{-1} exhibits two strong cross peaks (Figure 4(F)). We observed that the cross peaks present in the 2D vibrational map of 469 cm^{-1} agree with the spectral positions of vibrational progression (black dashed lines). This clearly delineates the vibrational origins within the 2DES framework. Additionally, the 2D vibrational maps corresponding to 938 cm^{-1} (displayed by using red contour lines in Figure 4(G)) further enabled the precise localization of the oscillatory origins of vibrational modes within the measured 2DES data.

Theoretical Calculations. To study the origin of these resolved vibrational coherences, we performed *ab initio* calculations (Gaussian 16 package[54] with the B3LYP functional[55] and the def2-TZVP basis set[56]) to characterize the electronic and vibrational properties of the molecule in gas phase. The geometry optimization was first performed for the singlet ground state from density functional theory (DFT) calculations with dispersion correction considered via the DFT-D3 method.[57] The resulting geometry exhibits D_3 symmetry, which is a subgroup of the O_h group for octahedral metal complexes. Therefore, compared to the highly degenerated $^1T_1$, $^3T_1$, and $^3T_2$ octahedral states, the excited states of the cobalt complex show slight splits. As shown in Figure 5(A), the three lowest singlet states (S_1, S_2, and S_3) show detectable oscillator strength. With A_1 symmetry, S_1 is found at 2.18 eV. By contrast, S_2 and S_3 are energetically degenerate at 2.23 eV with E symmetry. Below these singlet states, there are two branches of triplet states, which are well separated in energy. The higher energy branch (T_4, T_5, and T_6) has an energy around 1.6 eV, and the lower one (T_1, T_2, and T_3) is near 1.3 eV. Each branch of these triplets contains three triplet states. Similar to the singlet states, the lower triplet state (T_1 and T_4) within each branch has A_1 symmetry, while the higher two states (T_2 and T_3 for the lower branch, and T_5 and T_6 for the higher branch) have E symmetry and are energetically degenerate. As illustrated by the charge density difference (CDD, obtained using the Multiwfn program[58,59]) in Figure 5(A), there is no detectable charge transfer between the metal and the ligands during these transitions.

The vibrational modes of the optimized geometry were also obtained at the same level of theory, and the simulated Raman spectrum (Figure S3) was found to be in comparison with experimental measurements. We identified vibrational modes that showed significant resonance Raman intensity and coherent oscillations in our TG/2DES data. These are likely the modes most strongly displaced by LF excitation. Eighteen such candidate modes were considered (see SI Section X). We then computed the linear vibronic coupling parameters (diagonal tuning κ and off-diagonal coupling λ) for each mode and found that only a few modes exhibit particularly large couplings. Our model therefore focused on the two modes with the strongest effects: a high-frequency ∼950 cm^{-1} mode (dominantly tuning) and a low-frequency ∼195 cm^{-1} mode (dominantly coupling), while all other modes were treated as part of the dissipative bath. Raman activity was used only as an initial filter: modes with strong Raman intensity but negligible vibronic coupling were not included, whereas modes with modest Raman signal but very large coupling were included (SI Table S1). Along each mode, starting from the optimized geometry, a set of displaced conformations were obtained and were used for a separate excited state calculation. The resulting potential energy surfaces (PESs) for the adiabatic states along individual mode were then fitted to estimate the diagonal and off-diagonal electron−phonon coupling strengths of the mode. The vibrational mode characterization and excited state calculations for PES scan were performed using the ORCA[60] program. The resulting PES and the details for the fitting are given in the SI (Section X). Four key vibrational modes are found to exhibit relatively strong vibronic coupling, with the coupling strengths shown in Table 1 of SI. As illustrated by detailed molecular motions in Figure 5 (B), these modes mainly originated from the Co−O stretching movement and the bending of O−Co−O and C−CH−C. The corresponding 2D vibrational maps showed a mode of 217 cm^{-1}, which was assigned to the *ab initio* calculated mode of ∼200 cm^{-1}. The difference in the frequencies is mainly caused by the detection scheme (time step and total detection window) in TG and 2DES (details are in Sec. IX in SI). The SOC between the singlet and triplet states was calculated at the optimized ground state geometry at the same level of theory as implemented in ORCA.

In this way, we were able to construct a spin-vibronic coupling model with suitable SOC strengths and other refined parameters. The vibrational motions of key modes are selected with relatively strong vibronic coupling strengths, and the suitable vibrational levels were included in the model. The convolution of electronic and vibrational degrees of freedom results in a large-system Hamiltonian. For this, we employed GPU (RTX4090)-based hierarchy equation of motion (HEOM)[49,50] calculations to obtain population dynamics of ISC (Figure 5(C)) (optimized parameters are listed in the SI). Our pump pulse (620 nm) excites a manifold of closely spaced LF states (S_1−S_3). To reflect this, the initial density matrix in the HEOM simulation was partitioned roughly equally among

https://doi.org/10.1021/jacs.5c20395
J. Am. Chem. Soc. 2026, 148, 1977−1988

S_1, S_2, and S_3 (~33% each). The population dynamics under this broad initial excitation are qualitatively similar to the S_1-only case, although early time features differ since S_2 and S_3 quickly relax into S_1 prior to intersystem crossing. Importantly, the biphasic ISC behavior remains: a sub-200 fs, rapid component followed by a slower ~0.7 ps component are observed, consistent with our experimental kinetics. Interestingly, vibrational coherences are present at initial timepoints and decay on a timescale of 200 fs between the singlet excited states. Moreover, we also observed that the populations of the triplet states (T_4, T_5, and T_6) increase with the population time. In addition, T_4, which has the lowest site energy, shows a rapid increase in the amplitude within the calculation time window. We also extracted the population transfer timescales by fitting with exponential functions. The results show two lifetime components: 475 and 1514 fs. Importantly, these transfer time scales agree with our experimental observations revealed by the TG and 2DES measurements. The calculations also show vibrational coherences with time scales of ~200 fs, which is consistent with the vibrational coherences observed in the TG spectrum. We also performed an analysis of the vibrational coherence. For this, we used the time-resolved populations of each electronic singlet and triplet states, then applied a fitting procedure, and extracted the residuals for the coherence analysis (SI Sec. XVI). We performed a one-dimensional Fourier transform and plotted the identified vibrational mode at 950 cm^{-1}. The broad bandwidth of this peak indicates a relatively short lifetime, with a time scale of 50 ± 20 fs. This timescale agrees well with the experimental observations obtained from the TG and 2DES data. However, analysis of the vibrational coherence associated with the low-frequency 195 cm^{-1} mode cannot be effectively performed. We conclude that the mixed character of the 195 cm^{-1} mode (not a purely tuning or coupling mode) in our model is strongly coupled to the SOC, making the coherence highly complex and difficult to track using a simple model based on coherent transfer between two electronic states during the ISC process.

In order to examine the roles of the SOC and vibronic couplings, we artificially altered the strengths of the vibronic couplings and kept the other parameters as constants. For this, we changed the vibronic coupling strength of intramolecular vibration and calculated the population dynamics (Figure S14 in the SI). Population dynamics do not change significantly compared with the reference data (dashed lines). Moreover, we also calculated the population dynamics with changing value of λ (1.1 or 0.5 times of difference) (Figure S15 in the SI); transfer speed was significantly enhanced or reduced. Furthermore, we also examined the impact of SOC on population transfer. We altered the values of the SOC and recalculated the population dynamics between different electronic excited states (Figure S16). Again we observed that the transfer speed can be dramatically enhanced or reduced. Together, this demonstrated the importance of vibronic couplings (of the intramolecular coupling mode) and SOC for transitions between singlet and triplet states. We do not observe strong impact induced by vibronic coupling from κ since the optimized values in the system Hamiltonian are relatively small in comparison to other parameters. However, we cannot rule out the importance of vibronic couplings from κ of intramolecular vibrational modes since it could exist in the other molecular system with a similar physical process but a larger value.

To probe the influence of other vibrational coordinates, we performed additional HEOM simulations, including alternative mode pairs. Notably, replacing the 950 cm^{-1} mode with the ~460 cm^{-1} Co−O stretching mode (while keeping the 195 cm^{-1} mode) still yields efficient ISC, albeit with a slightly longer timescale. Similarly, a model with the 262 cm^{-1} mode (again +195 cm^{-1} mode) shows only modest changes. These tests (see SI Section XIII) indicate that other low-frequency metal−ligand modes can also drive ISC, and if multiple modes could be included simultaneously, their combined effect might accelerate ISC even further. While a full multimode simulation is computationally very expensive, this two-mode model suggests a tractable representation capturing the dominant contributions.

DISCUSSION

Our combined experimental and theoretical results provide a clear mechanistic picture of ultrafast ISC in $[Co(acac)_3]$ upon ligand-field excitation. We find that vibrational motion plays a decisive role in enabling a spin-forbidden transition on subpicosecond time scales. Ultrafast vibrational coherences (observable as ~50 fs oscillations in our TG and 2DES measurements) accompany and facilitate the initial S → T population transfer. These coherent nuclear dynamics prepare the system for ISC by rapidly modulating the excited-state potential energy surfaces. As a result, two distinct ISC time scales emerge: an initial fast component on the order of a few hundred femtoseconds, followed by a second, slower phase (~0.7−1 ps) before the triplet population fully stabilizes. The fast phase corresponds to vibrationally driven crossing from the singlet state manifold to higher triplet states, while the ~750 fs component reflects the residual population transfer into the lowest-energy triplet (and/or vibrational cooling within the triplet manifold). These timescales, extracted from global kinetic fitting of the data (see SI), are in excellent agreement with our HEOM simulations. The agreement between experiment and theory (in both the transient vibrational frequencies and biphasic kinetics) lends strong support to the proposed mechanism.

At the molecular level, our results indicate that ultrafast ISC in this Co(III) complex follows a spin-vibronic mechanism governed by a synergy between vibrational coupling and the spin−orbit interaction. In essence, nuclear vibrations drive the system toward regions of near-degeneracy between the singlet and triplet potential energy surfaces, while SOC provides the route for spin flip once those surfaces are sufficiently mixed. We identify a ~195 cm^{-1} Co−O−C bending mode as a key "coupling mode" that strongly mixes the $^1T_1$ (singlet state, S) and ^3T (triplet state, T) characters via off-diagonal vibronic coupling λ. When this mode is active, the energy gap between singlet and triplet states oscillates, and occasional S/T crossings (or avoided crossings) occur, effectively quenching the spin-forbidden nature of the transition. The importance of this low-frequency mode is confirmed by HEOM simulations in which we varied its vibronic coupling strength: increasing λ (by 10%) markedly accelerates the S → T transfer, whereas reducing it (to ~50%) slows the ISC correspondingly. Even with Co(III)'s relatively modest SOC, such strong vibronic perturbation along selective coordinates compensates to achieve a high ISC rate. By contrast, a high-frequency ~950 cm^{-1} Co−O/C−C stretching mode acts primarily as a "tuning mode", modulating the energy separation (diagonal coupling κ) of the states. Its influence on ISC is much smaller (adjusting

https://doi.org/10.1021/jacs.5c20395
J. Am. Chem. Soc. 2026, 148, 1977−1988

the 950 cm^{-1} mode's coupling has little effect on the transfer rate in our tests) because its equilibrium displacement (and thus κ) in this system is modest. In other words, the 950 cm^{-1} mode helps prepare the electronic wave functions (via energy redistribution), but it is the 195 cm^{-1} mode that most efficiently drives the wave function mixing needed for ISC. Importantly, the spin−orbit interaction must still be present to allow population to effectively change spin multiplicity. In line with expectation, we find that artificially enhancing the SOC (e.g., doubling the SOC matrix elements) makes ISC almost instant, whereas halving the SOC slows the triplet yield dramatically. These simulation outcomes, summarized in Figure 5(C) (main text) and Figure S16 (SI), now underscore that both ingredients (vibrational motion and SOC) are necessary and together sufficient for ultrafast ISC. Vibronic coupling (predominantly via the 195 cm^{-1} mode) brings the singlet and triplet states into intimate contact, and SOC then provides the pathway for population to move onto the triplet surface.

Our spin-vibronic model thus answers the question: "How does ISC occur so quickly in a first-row complex with weak SOC?". It occurs through vibrationally accelerated intersystem crossing. A vibrational wavepacket launched on the excited singlet surface immediately begins to distort the molecule along key coordinates (e.g., Co−O stretches and bends), searching out a crossing to the triplet surface. Within ∼100−200 fs, the wavepacket encounters a region of strong singlet−triplet coupling, essentially a transient funnel or avoided crossing between the surfaces at which point even a moderate SOC (augmented by the vibronic mixing) allows the population to hop to the triplet state. This mechanism can be visualized as a concerted dance of electrons and nuclei: the nuclei move in just the right way (coherently at first) to break the spin-selection rule, and the electrons respond by flipping spin. Our HEOM simulations (Figure 5(C)) explicitly capture this process, including the initial quantum coherence between states and its eventual decay due to vibrational dephasing and environmental damping. Indeed, the calculated vibrational coherence lifetime (∼200 fs) closely matches the experimentally observed coherence decay in the TG spectra, an agreement attributable to our inclusion of dissipation in the model. (By contrast, wavepacket propagation on an isolated, nondissipative PES might overestimate coherence lifetimes.) We note that while sophisticated wavepacket methods such as multiconfiguration time-dependent Hartree (MCTDH)[61,62] could in principle include many vibrational modes explicitly, they do not easily incorporate finite-temperature damping. Our open-quantum-system approach (HEOM) treats the solvent/bath degrees of freedom, ensuring that the simulated decoherence and energy relaxation are realistic. This is vital for quantitatively reproducing the ∼50−100 fs coherence decays and the kinetics of population transfer in solution. It should be noted that our spin-vibronic HEOM framework captures the modulation of electronic mixing arising from vibronic coupling within and between electronic manifolds, while acknowledging that vibrational modulation of the SOC matrix elements themselves constitutes a separate, mode-dependent contribution.[30]

Finally, we consider the broader implications of this coherent spin-vibronic ISC mechanism. Our results now show that even in a "simple" ligand-field excited d^6 complex, multiple vibrational motions coordinate to assist what would otherwise be a slow, spin-forbidden transition. Our two-mode model captured the dominant effects with one coupling mode and one tuning mode, but additional low-frequency vibrations (e.g., the ∼460 cm^{-1} Co−O stretching mode) are also expected to participate. Test simulations including the 460 cm^{-1} mode (see SI) indicate that it can further promote ISC (although adding many modes simultaneously lies beyond current computational capabilities). We accordingly note that entire coordination sphere breathing likely contributes to ultrafast ISC in $[Co(acac)_3]$, not just a single mode. From a design perspective, this means that tuning a complex's vibrational spectrum (through ligand rigidity, symmetry, or isotopic substitution) offers a strategy to control ISC rates. For example, strengthening metal−ligand bonds or lowering symmetry could enhance certain vibronic couplings and thus accelerate (or decelerate) ISC as needed. More generally, our findings underline that vibronic coupling can effectively compensate for weak SOC in first-row complexes. By exploiting vibrations to mediate spin transitions, these systems achieve surprisingly fast ISC, approaching the performance typically associated with heavy-metal complexes.

This insight now expands our understanding of photophysical design rules: it is not only the magnitude of SOC (dictated by the metal's atomic number) that matters but also the vibrational architecture of the complex. Harnessing the right vibrational motions can open up efficient spin-crossing pathways, even when SOC alone would be insufficient. Such 'vibronic engineering' parallels structural control strategies recently demonstrated in Co(III) systems.[63] The broader significance of this framework is underscored by recent significant studies where ligand-field control has revealed inverted-region excited-state behavior, and shown that LF states themselves can drive potent oxidative chemistry.[36,40] Together, these advances highlight that controlling vibrational contributions to ISC is a powerful, generalizable route to the rational design of next-generation, earth-abundant photocatalysts. In summary, a coherent spin-vibronic mechanism for ultrafast ISC in $[Co(acac)_3]$ integrates experimental observations and theoretical results to show that vibrational energy flow and spin conversion are intertwined at every step, providing a clear answer to the puzzle of how a d-block complex with only moderate SOC can undergo ISC in under a picosecond.

EXPERIMENTAL SECTION

Sample Preparation. The cobalt complex, $[Co(acac)_3]$, used in this study was procured from YuanYe Bio (website: https://www.shyuanye.com) and was utilized without any further chemical modifications. The complex was initially dissolved in acetonitrile and subsequently diluted to achieve a maximum optical density (OD) of 0.3 at 620 nm, as measured by its absorption spectrum. To circulate the sample through the flow cell, we employed a Micropump GA-X21-DEMSE system. The sample path length within the flow cell was maintained at 0.5 mm, regulated by a dedicated power supply. A custom-built XYZ delay-stage system was developed to precisely control the laser beam focus on the sample. This setup allowed us to optimize the sample alignment and beam spot size, ensuring ideal spatial positioning for TA, TG, and 2DES measurements. By minimizing scattering, we were able to significantly enhance the signal-to-noise ratio. Detailed descriptions of the laser system, spectroscopic configurations, noncollinear optical parametric amplifier (NOPA), and TG spectrometer setups are provided in the following section.

TA, TG, and 2DES Measurements with Experimental Conditions. Details of the experimental setup have been described in earlier reports from our group.[51,52] Briefly, the measurements have

https://doi.org/10.1021/jacs.5c20395
J. Am. Chem. Soc. 2026, 148, 1977−1988

been performed on diffractive optics based on an all-reflective 2D spectrometer with a phase stability of $\lambda/160$. The laser beam from a home-built NOPA (pumped by a commercial femtosecond Spectra Physics laser from Newport) is compressed to ~10 fs using the combination of a deformable mirror (OKO Technologies, 19 channels) and a prism pair (FS materials). Frequency-resolved optical grating (FROG) measurement is used to characterize the temporal profile of the compressed beam, and the obtained FROG traces are evaluated using a commercial program FROG3 (Femtosecond Technologies). An obtained broadband spectrum carried a line width of ~120 nm (fwhm) centered at 620 nm, which covered the electronic transitions to the first excited state. For the 2DES measurement, three pulses are focused on the sample with a spot size of ~130 μm and the photon echo signal is generated at the phase-matching direction. The photon echo signals are collected using Sciencetech spectrometer model 9055F, which is coupled to a CCD linear array camera (Entwicklungsbüro Stresing). TA and TG spectra were recorded for each waiting time T by scanning the delay time over the range of [-200 fs, 3 ps] in 3 fs increments. To minimize noise, 200 spectra were averaged at each delay point. In the 2DES measurements, the coherence time τ was scanned across a time window of [-64, 64] fs. The waiting time was varied from 0 to 2 ps in 15 fs steps. During all experiments, the excitation pulse energy was reduced to 10 nJ and operated at a repetition rate of 1 kHz. The TG and 2DES spectra were phased using the "invariant theorem" as detailed in ref 53.

Theoretical Calculations. The optimized molecular geometry is first obtained for the singlet ground state and is then used for the calculations of normal modes and Raman spectrum using DFT. According to the Raman activities, 18 normal modes are selected to displace the molecule for PES calculations. Along each mode, 40 displaced molecular configurations are generated and used for excited state calculations, where the 10 lowest-rank singlets and triplets are included. The diagonal and off-diagonal vibronic couplings for each mode are obtained by fitting the adiabatic PESs using a vibronic Hamiltonian. The spin−orbital couplings are evaluated at the optimized singlet ground state geometry.0

Additionally, we performed multireference NEVPT2/CASSCF-(6,5) calculations to benchmark the TDDFT results. The first excited LF singlet energy predicted by CASSCF (~2.5 eV) is consistent with our TDDFT value (~2.2 eV) and close to the experimental $^1A_1 \rightarrow {}^1T_1$ absorption (~2.4 eV in solution). We also compared SOC matrix elements from DFT and CASSCF; the values agree closely (see Table S2 in the Supporting Information), confirming that our DFT-derived SOC parameters are robust.

Based on the *ab initio* calculations, we were able to construct a spin-vibronic coupling model for the cobalt complex. The system Hamiltonian can be written as

$$H_s = \sum_{i=1}^{N} |e_i\rangle(\epsilon_i + h_i)\langle e_i| + \sum_{i\neq j} |e_i\rangle(V_{ij} + \lambda_{ij}Q_c)\langle e_j|,$$
$$h_i = \frac{1}{2}\hbar\Omega_t\left(\alpha_t^{\dagger}\alpha_t + \frac{1}{2}\right) + \frac{1}{2}\hbar\Omega_c\left(\alpha_c^{\dagger}\alpha_c + \frac{1}{2}\right) + \kappa_i Q_t \quad (1)$$

where $|e_i\rangle$ is the electronic singlet or triplet states. Here, it denotes S_1, S_2, S_3, T_4, T_5 and T_6, respectively. Thus, $N = 6$ in this work. V_{ij} and λ_{ij} are the parameters of excitonic couplings and vibronic couplings of the intermolecular vibrations, respectively. Moreover, κ_i is the parameter determining the vibronic coupling of intramolecular vibration. It shows the relation $\kappa_i = \Delta_i\Omega_t/\sqrt{2}$, where Δ_i is the dimensionless shift of the minimum position of the i-th potential energy surface compared to the position of the ground electronic state. Ω_t and Ω_c are the frequencies of the tuning and coupling modes. In this work, we employed the system-bath model to consider the dissipation and relation acted by noisy environment. Thus, we have $H = H_s + H_{env}$ and the environment can be considered as an infinity number of harmonic oscillators that act as a thermal reservoir. The environmental bath Hamiltonian is given as

$$H_{env} = \sum_{\alpha}\left[\frac{p_\alpha^2}{2m_\alpha} + \frac{m_\alpha\omega_\alpha^2}{2}\left(x_\alpha + \frac{c_\alpha Q_c}{m_\alpha\omega_\alpha^2}\right)^2 + \frac{q_\alpha^2}{2M_\alpha} + \frac{M_\alpha\nu_\alpha^2}{2}\left(y_\alpha + \frac{t_\alpha Q_t}{M_\alpha\nu_\alpha^2}\right)^2\right] \quad (2)$$

Here, the momenta of the bath oscillators are denoted as p_α and q_α, while their coordinates, masses, and frequencies are denoted by x_α, m_α, ω_α, and y_α, M_α, ν_α. The respective coupling constants are c_α and t_α. The baths are characterized by the spectral densities $J_c(\omega) = \frac{\pi}{2}\sum_\alpha \frac{c_\alpha^2}{m_\alpha\omega_\alpha}\delta(\omega - \omega_\alpha)$ and $J_t(\omega) = \frac{\pi}{2}\sum_\alpha \frac{t_\alpha^2}{M_\alpha\nu_\alpha}\delta(\omega - \nu_\alpha)$. Throughout this work, we assume two Lorentzian types of spectral density $J_{c/t}(\omega) = 2\lambda_{t/c}\frac{\omega\gamma}{\omega^2+\gamma^2}$, with $\lambda_{t/c} = \frac{\zeta_{t/c}\gamma}{2\pi}$, where λ is the reorganization energy of bath, and we assume the same value for each bath. $\zeta_{t/c}$ and γ are the coupling and cutoff frequencies of each bath, respectively. The model parameters were obtained based on the *ab initio* calculations, and the detailed values of the parameters are described in the SI.

■ ASSOCIATED CONTENT

Supporting Information

The Supporting Information is available free of charge at https://pubs.acs.org/doi/10.1021/jacs.5c20395.

Details of global fitting approach; fitting procedure of residuals; wavelet analysis; calculated and measured Raman spectra; theoretical model; and calculations of population dynamics (PDF)

■ AUTHOR INFORMATION

Corresponding Authors

Fulu Zheng − *Department of Physics, School of Physical Science and Technology, Ningbo University, Ningbo 315211, P. R. China;* orcid.org/0000-0003-3439-1575; Email: zhengfulu@nbu.edu.cn

Hong-Guang Duan − *Department of Physics, School of Physical Science and Technology, Ningbo University, Ningbo 315211, P. R. China;* orcid.org/0000-0001-6589-0890; Email: duanhongguang@nbu.edu.cn

Ajay Jha − *Rosalind Franklin Institute, Harwell, Oxfordshire OX11 0QX, U.K.; Department of Pharmacology, University of Oxford, Oxford OX1 3QT, U.K.; Research Complex at Harwell, Rutherford Appleton Laboratory, Didcot OX11 0QX, U.K.;* orcid.org/0000-0002-4489-518X; Email: ajay.jha@rfi.ac.uk

Authors

Jing Yang − *Department of Physics, School of Physical Science and Technology, Ningbo University, Ningbo 315211, P. R. China*

Panpan Zhang − *Department of Physics, School of Physical Science and Technology, Ningbo University, Ningbo 315211, P. R. China*

Zihui Liu − *Department of Physics, School of Physical Science and Technology, Ningbo University, Ningbo 315211, P. R. China*

Michael Penny − *Rosalind Franklin Institute, Harwell, Oxfordshire OX11 0QX, U.K.;* orcid.org/0009-0003-8788-8814

Sara Mosca − *Central Laser Facility, Research Complex at Harwell, STFC Rutherford Appleton Laboratory, UK*

https://doi.org/10.1021/jacs.5c20395
J. Am. Chem. Soc. 2026, 148, 1977−1988

Research and Innovation (UKRI), Harwell, Oxford OX11 0QX, U.K.; orcid.org/0000-0001-9479-5614

Junhua Zhou − *Department of Physics, School of Physical Science and Technology, Ningbo University, Ningbo 315211, P. R. China*

Vandana Tiwari − *Stanford PULSE Institute, SLAC National Accelerator Laboratory, Menlo Park, California 94025, United States; Department of Chemical Science, Linac Coherent Light Source, SLAC National Accelerator Laboratory, Menlo Park, California 94025, United States; Molecular Biophysics and Integrated Bioimaging Division, Lawrence Berkeley National Laboratory, Berkeley, California 94729, United States*

Benjamin G. Davis − *Rosalind Franklin Institute, Harwell, Oxfordshire OX11 0QX, U.K.; Department of Pharmacology, University of Oxford, Oxford OX1 3QT, U.K.; Department of Chemistry, University of Oxford, Oxford OX1 3TA, U.K.;* orcid.org/0000-0002-5056-407X

Complete contact information is available at: https://pubs.acs.org/10.1021/jacs.5c20395

Author Contributions

¶J.Y., P.Z., and Z.L. contributed equally to this work.

Notes

The authors declare no competing financial interest.

■ ACKNOWLEDGMENTS

This work was supported by the National Key Research and Development Program of China (Grant No. 2024YFA1409800), NSFC Grant with No. 12274247, 12504279 12404310 and W2421021, Yongjiang talents program with No. 2022A-094-G and 2023A-158-G, Ningbo International Science and Technology Cooperation with No. 2023H009, "Lixue+" Innovation Leading Project, and the Foundation of National Excellent Young Scientist.

■ REFERENCES

(1) Twilton, J.; Le, C.; Zhang, P.; et al. The merger of transition metal and photocatalysis. *Nat. Rev. Chem.* **2017**, *1*, No. 0052.

(2) Arias-Rotondo, D. M.; McCusker, J. K. The photophysics of photoredox catalysis: a roadmap for catalyst design. *Chem. Soc. Rev.* **2016**, *45*, 5803−5820.

(3) Förster, C.; Heinze, K. Photophysics and photochemistry with Earth-abundant metals-fundamentals and concepts. *Chem. Soc. Rev.* **2020**, *49*, 1057−1070.

(4) Xu, H.; Chen, R.; Sun, Q.; et al. Recent progress in metal-organic complexes for optoelectronic applications. *Chem. Soc. Rev.* **2014**, *43*, 3259−3302.

(5) de Groot, L. H. M.; Ilic, A.; Schwarz, J.; Wärnmark, K. Iron Photoredox Catalysis-Past, Present, and Future. *J. Am. Chem. Soc.* **2023**, *145*, 9369−9388.

(6) McKenzie, L. K.; Bryant, H. E.; Weinstein, J. A. Transition metal complexes as photosensitisers in one- and two-photon photodynamic therapy. *Coord. Chem. Rev.* **2019**, *379*, 2−29.

(7) Karges, J. Clinical Development of Metal Complexes as Photosensitizers for Photodynamic Therapy of Cancer. *Angew. Chem., Int. Ed.* **2022**, *61*, No. e202112236.

(8) Monro, S.; Colón, K. L.; Yin, H.; et al. Transition Metal Complexes and Photodynamic Therapy from a Tumor-Centered Approach: Challenges, Opportunities, and Highlights from the Development of TLD1433. *Chem. Rev.* **2019**, *119*, 797−828.

(9) Marian, C. M. Understanding and Controlling Intersystem Crossing in Molecules. *Annu. Rev. Phys. Chem.* **2021**, *72*, 617−640.

(10) Chergui, M. Ultrafast Photophysics of Transition Metal Complexes. *Acc. Chem. Res.* **2015**, *48*, 801−808.

(11) Daniel, C. Photochemistry and photophysics of transition metal complexes: Quantum chemistry. *Coord. Chem. Rev.* **2015**, *282*−*283*, 19−32.

(12) Gaffney, K. J. Capturing photochemical and photophysical transformations in iron complexes with ultrafast X-ray spectroscopy and scattering. *Chem. Sci.* **2021**, *12*, 8010−8025.

(13) Oppermann, M.; Zinna, F.; Lacour, J.; Chergui, M. Chiral control of spin-crossover dynamics in Fe(II) complexes. *Nat. Chem.* **2022**, *14*, 739−745.

(14) Katayama, T.; Penfold, T. J.; Bressler, C. *Ultrafast Electronic and Structural Dynamics*; Ueda, K., Ed.; Springer Nature: Singapore, 2024; pp 253−267.

(15) Chen, L. X. *Comprehensive Inorganic Chemistry III*, 3rd ed.; Reedijk, J.; Poeppelmeier, K. R., Eds.; Elsevier, 2023; pp 679−706.

(16) Jiang, Y.; Liu, L. C.; Sarracini, A.; et al. Direct observation of nuclear reorganization driven by ultrafast spin transitions. *Nat. Commun.* **2020**, *11*, No. 1530.

(17) Jiang, Y.; Hayes, S.; Bittmann, S.; et al. Direct observation of photoinduced sequential spin transition in a halogen-bonded hybrid system by complementary ultrafast optical and electron probes. *Nat. Commun.* **2024**, *15*, No. 4604.

(18) Wenger, O. S. Photoactive Complexes with Earth-Abundant Metals. *J. Am. Chem. Soc.* **2018**, *140*, 13522−13533.

(19) McCusker, J. K. Electronic structure in the transition metal block and its implications for light harvesting. *Science* **2019**, *363*, 484−488.

(20) Juban, E. A.; Smeigh, A. L.; Monat, J. E.; McCusker, J. K. Ultrafast dynamics of ligand-field excited states. *Coord. Chem. Rev.* **2006**, *250*, 1783−1791.

(21) Sinha, N.; Wenger, O. S. Photoactive Metal-to-Ligand Charge Transfer Excited States in 3d6 Complexes with Cr0, MnI, FeII, and CoIII. *J. Am. Chem. Soc.* **2023**, *145*, 4903−4920.

(22) Hossain, A.; Bhattacharyya, A.; Reiser, O. Copper's rapid ascent in visible-light photoredox catalysis. *Science* **2019**, *364*, No. eaav9713.

(23) Lazorski, M. S.; Castellano, F. N. Advances in the light conversion properties of Cu(I)-based photosensitizers. *Polyhedron* **2014**, *82*, 57−70.

(24) Housecroft, C. E.; Constable, E. C. The emergence of copper(i)-based dye sensitized solar cells. *Chem. Soc. Rev.* **2015**, *44*, 8386−8398.

(25) Mara, M. W.; Fransted, K. A.; Chen, L. X. Interplays of excited state structures and dynamics in copper(I) diimine complexes: Implications and perspectives. *Coord. Chem. Rev.* **2015**, *282*−*283*, 2−18.

(26) Iwamura, M.; Takeuchi, S.; Tahara, T. Ultrafast Excited-State Dynamics of Copper(I) Complexes. *Acc. Chem. Res.* **2015**, *48*, 782−791.

(27) Tiwari, V.; Gallagher-Jones, M.; Hwang, H.; et al. Crystal Lattice-Induced Stress modulates Photoinduced Jahn−Teller Distortion Dynamics. *ACS Phys. Chem. Au* **2024**, *4*, 660−668, DOI: 10.1021/acsphyschemau.4c00047.

(28) Carey, M. C.; Sara, L. A.; McCusker, J. K. Insights into the excited state dynamics of Fe(ii) polypyridyl complexes from variable-temperature ultrafast spectroscopy. *Chem. Sci.* **2019**, *10*, 134−144.

(29) Hong, K.; Cho, H.; Schoenlein, R. W.; Kim, T. K.; Huse, N. Element-Specific Characterization of Transient Electronic Structure of Solvated Fe(II) Complexes with Time-Resolved Soft X-ray Absorption Spectroscopy. *Acc. Chem. Res.* **2015**, *48*, 2957−2966.

(30) Penfold, T. J.; Gindensperger, E.; Daniel, C.; et al. Spin-Vibronic Mechanism for Intersystem Crossing. *Chem. Soc. Rev.* **2018**, *118* (15), 6975−7025.

(31) Daniel, C. Ultrafast processes: coordination chemistry and quantum theory. *Phys. Chem. Chem. Phys.* **2021**, *23*, 43−58.

(32) Fumanal, M.; Daniel, C.; Gindensperger, E.; et al. Excited-state dynamics of [Mn(im)(CO)3(phen)]+: PhotoCORM, catalyst, luminescent probe? *J. Chem. Phys.* **2021**, *154*, No. 154102.

(33) Mandal, S.; Daniel, C. Spin−vibronic mechanism at work in a luminescent square-planar cyclometalated tridentate Pt(ii) complex:

absorption and ultrafast photophysics. *Phys. Chem. Chem. Phys.* **2023**, *25*, 18720−18727.
(34) Yarranton, J. T.; McCusker, J. K. Ligand-Field Spectroscopy of Co(III) Complexes and the Development of a Spectrochemical Series for Low-Spin d6 Charge-Transfer Chromophores. *J. Am. Chem. Soc.* **2022**, *144*, 12488−12500.
(35) Kalsi, D.; Dutta, S.; Barsu, N.; Rueping, M.; Sundararaju, B. Room-Temperature C−H Bond Functionalization by Merging Cobalt and Photoredox Catalysis. *ACS Catal.* **2018**, *8*, 8115−8120.
(36) Chan, A. Y.; Ghosh, A.; Yarranton, J. T.; et al. Exploiting the Marcus inverted region for first-row transition metal−based photoredox catalysis. *Science* **2023**, *382*, 191−197.
(37) Sinha, N.; Pfund, B.; Wegeberg, C.; Prescimone, A.; Wenger, O. S. Cobalt(III) Carbene Complex with an Electronic Excited-State Structure Similar to Cyclometalated Iridium(III) Compounds. *J. Am. Chem. Soc.* **2022**, *144*, 9859−9873.
(38) Ferrari, L.; Satta, M.; Palma, A.; et al. A Fast Transient Absorption Study of Co(AcAc)3. *Front. Chem.* **2019**, *7*, No. 348, DOI: 10.3389/fchem.2019.00348.
(39) McCusker, J. K.; Walda, K. N.; Magde, D.; Hendrickson, D. N. Picosecond excited-state dynamics in octahedral cobalt(III) complexes: intersystem crossing versus internal conversion. *Inorg. Chem.* **1993**, *32*, 394−399.
(40) Ghosh, A.; Yarranton, J. T.; McCusker, J. K. Establishing the origin of Marcus-inverted-region behaviour in the excited-state dynamics of cobalt(III) polypyridyl complexes. *Nat. Chem.* **2024**, *16*, 1665−1672.
(41) Duan, H.-G.; Jha, A.; Li, X.; et al. Intermolecular vibrations mediate ultrafast singlet fission. *Sci. Adv.* **2020**, *6*, No. eabb0052.
(42) Duan, H.-G.; Tiwari, V.; Jha, A.; et al. Photoinduced Vibrations Drive Ultrafast Structural Distortion in Lead Halide Perovskite. *J. Am. Chem. Soc.* **2020**, *142*, 16569−16578.
(43) Biswas, S.; Kim, J.; Zhang, X.; et al. Coherent Two-Dimensional and Broadband Electronic Spectroscopies. *Chem. Rev.* **2022**, *122*, 4257−4321.
(44) Fuller, F. D.; Ogilvie, J. P. Experimental Implementations of Two-Dimensional Fourier Transform Electronic Spectroscopy. *Annu. Rev. Phys. Chem.* **2015**, *66*, 667−690.
(45) Collini, E. 2D Electronic Spectroscopic Techniques for Quantum Technology Applications. *J. Phys. Chem. C* **2021**, *125*, 13096−13108.
(46) Jha, A.; Duan, H. G.; Tiwari, V.; et al. Origin of poor doping efficiency in solution processed organic semiconductors. *Chem. Sci.* **2018**, *9*, 4468−4476.
(47) Duan, H.-G.; Jha, A.; Chen, L.; et al. Quantum coherent energy transport in the Fenna-Matthews-Olson complex at low temperature. *Proc. Natl. Acad. Sci. U.S.A.* **2022**, *119*, No. e2212630119.
(48) Jha, A.; Duan, H. G.; Tiwari, V.; et al. Direct Observation of Ultrafast Exciton Dissociation in Lead Iodide Perovskite by 2D Electronic Spectroscopy. *ACS Photonics* **2018**, *5*, 852−860.
(49) Tsuchimoto, M.; Tanimura, Y. Spins Dynamics in a Dissipative Environment: Hierarchal Equations of Motion Approach Using a Graphics Processing Unit (GPU). *J. Chem. Them. Comp.* **2015**, *11*, 3859−3865.
(50) Ishizaki, A.; Tanimura, Y. Quantum Dynamics of System Strongly Coupled to Low-Temperature Colored Noise Bath: Reduced Hierarchy Equations Approach. *J. Phys. Soc. Jpn.* **2005**, *74*, 3131−3134.
(51) Jha, A.; Zhang, P. P.; Tiwari, V.; et al. Unraveling quantum coherences mediating primary charge transfer processes in photosystem II reaction center. *Sci. Adv.* **2024**, *10*, No. adk1312.
(52) Zhang, X.; Zhou, J.; Zheng, F.; et al. Ultrafast exciton-phonon coupling and energy transfer dynamics in quasi-2D layered Ruddlesden-Popper perovskites. *Commun. Phys.* **2025**, *8*, No. 71.
(53) Hybl, J. D.; Ferro, A. A.; Jonas, D. M. Two-dimensional Fourier transform electronic spectroscopy. *J. Chem. Phys.* **2001**, *115*, 6606−6622.
(54) *Gaussian 16 Rev. C.01*; Gaussian: Wallingford, CT, 2016.
(55) Becke, A. Density-Functional, D. Thermochemistry 0.3. The Role of Exact Exchange. *J. Chem. Phys.* **1993**, *98*, 5648−5652.
(56) Weigend, F.; Ahlrichs, R. Balanced basis sets of split valence, triple zeta valence and quadruple zeta valence quality for H to Rn: Design and assessment of accuracy. *Phys. Chem. Chem. Phys.* **2005**, *7*, 3297−3305.
(57) Grimme, S.; Antony, J.; Ehrlich, S.; Krieg, H. A consistent and accurate ab initio parametrization of density functional dispersion correction (DFT-D) for the 94 elements H-Pu. *J. Chem. Phys.* **2010**, *132*, No. 154104.
(58) Lu, T.; Chen, F. Multiwfn: A Multifunctional Wavefunction Analyzer. *J. Comput. Chem.* **2012**, *33*, 580−592.
(59) Lu, T. A comprehensive electron wavefunction analysis toolbox for chemists, Multiwfn. *J. Chem. Phys.* **2024**, *161*, No. 082503.
(60) Neese, F. Software update: the ORCA program system, version 5.0. *WIRES Comput. Mol. Sci.* **2022**, *12*, No. e1606.
(61) Meyer, H.-D.; Gatti, F.; Worth, G. A. *Multidimensional Quantum Dynamics: MCTDH Theory and Applications*; Wiley-VCH Verlag GmbH & Co. KGaA, 2009.
(62) Beck, M. H. The multiconfiguration time-dependent Hartree (MCTDH) method: a highly efficient algorithm for propagating wavepackets. *Phys. Rep.* **2000**, *324*, 1−105.
(63) Yaltseva, P.; Maisuradze, T.; Prescimone, A.; et al. Structural Control of Metal-Centered Excited States in Cobalt(III) Complexes via Bite Angle and π-π Interactions. *J. Am. Chem. Soc.* **2025**, *147* (32), 29444−29456.

https://doi.org/10.1021/jacs.5c20395
J. Am. Chem. Soc. 2026, 148, 1977−1988